Modelling Alongshore Currents over Barred Beaches

Stuart McIlwain[1] and Donald N. Slinn[2]

Abstract

The nonlinear dynamics of alongshore currents in the surf zone over an alongshore-uniform barred beach topography are studied using numerical experiments. The simulations use finite difference solutions to the nonlinear shallow water equations for forced, dissipative, initial value problems. The simulations are performed with and without wave-current interaction, and incorporate different formulations for linear or non-linear bottom friction parameterizations. The alongshore currents are forced by the momentum input from breaking surface waves, which is calculated using either the Thornton-Guza type sub-model, or a new two-dimensional time-dependent roller model for obliquely incident waves. The results are compared to averaged field data measured on a natural barred beach during the Delilah experiment. The choice of the wave-breaking model has a greater effect on the predicted alongshore currents than the choice of the bottom friction model. Wave-current interaction affects the magnitude

[1]Institute for Aerospace Research, National Research Council of Canada, Ottawa, ON, K1A 0R6, CANADA, E-mail: Stuart.McIlwain@nrc-cnrc.gc.ca

[2]Department of Civil and Coastal Engineering, University of Florida, Gainesville, FL, 32611-6590, USA, E-mail: Slinn@coastal.ufl.edu

but not the location of the mean alongshore currents. Data from simulations that used non-linear bottom friction and a roller model most closely resemble the field data.

Keywords: numerical model, nearshore, current, beaches, breaking waves

1 Introduction

Alongshore currents are generated as obliquely-incident surface waves break in shallow water and wave momentum is transferred into the water column. Observations in the nearshore surf zone at Duck, North Carolina, by Oltman-Shay *et al.* (1989) identified propagating disturbances associated with the presence of alongshore currents. Bowen & Holman (1989) interpreted the disturbances as shear instabilities of the mean currents. To better understand the nearshore flow dynamics that caused the disturbances, Allen *et al.* (1996) developed a numerical model based on the two-dimensional depth-averaged time-dependent shallow water equations with idealized forcing to study the nonlinear shear waves on plane beaches. The model was extended to include barred beaches by Slinn *et al.* (1998) and alongshore variable beaches by Slinn *et al.* (2000). These studies focused on the dependence of the general characteristics of the flow on the magnitude of the modelled bottom friction, wave field properties, and did not pursue detailed comparisons with field data. Therefore, simple bottom stress and wave-breaking models were used, and the influences of these parameterizations were not investigated.

Recently, several groups of researchers have attempted to improve the parameterizations used in alongshore current models. For example, Feddersen *et al.* (2000) reviewed several bottom stress parameterizations and compared their predictions to time series of near-bottom current field data in the nearshore region. They showed that linear parameterizations cause numerical models to underestimate the bottom friction. The best parameterization was based on a joint-Gaussian velocity field, but several non-linear parameterizations were deemed adequate for modelling purposes.

In other studies, a one-dimensional roller model was added to improve the wave-forcing parameterization (see Reniers & Battjes, 1997; Lippmann *et al.* , 1996; Nairn *et al.* , 1990). Yu & Slinn (2003) added wave-current interaction to the Slinn *et al.* (2000) model by including two-way coupling between the partial differential equations for the shoaling wave energy and the shallow water equations through the radiation stresses. The new model was used to study rip currents over an alongshore-variable beach bathymetry. They showed that wave-current interaction provides negative feedback to the wave forcing, thereby reducing the strength and offshore extent of the rip currents.

One purpose of the present work is to improve the alongshore current predictions of the Slinn *et al.* (2000) model, and to compare those predictions to the Delilah field experiment data measured in October, 1990, at Duck, North Carolina. The numerical experiments of Slinn *et al.* (2000) focused on the flow response to alongshore topographic variability and examined the roles of alongshore pressure gradients and spatial variations in the radiation stress gradients. They found that for a variety of alongshore topographic length scales, bottom friction coefficients, and incident wave conditions, that the modelled alongshore current profiles were qualitatively different from alongshore currents observed at the Duck field experiments. In particular, the previous combinations of modelling approximations were unable to produce a peak current located shoreward of the sand bar and produced an artificially large shore-parallel current close to the shore line. There are a wide variety of modelling choices that can be invoked in nearshore circulation models, and different modelling groups have chosen different approaches. In the present paper, we focus on gaining a better quantitative understanding of some of these choices. Our study is not exhaustive,

and related investigations are being conducted at other institutions focusing on other details. For example, Bühler & Jacobson (2001) investigated the effect of a nonhomogeneous wavetrain, which is not considered here. There is strong international interest in near shore circulation modelling because of the societal relevance to shoreline erosion, sediment transport, dispersal of pollutants, and other coastal and marine environmental issues.

Here, we examine the influence of six different model features: utilizing 1) four bottom friction formulations (at any given value of friction coefficient), 2) three types of horizontal mixing, 3) the influence of wave-current interaction, 4) two offshore wave field conditions, 5) two wave breaking energy dissipation parameterizations, and 6) five types of roller models. At this degree of variation, there are 480 combinations of these six features (for a single bottom friction coefficient), and over the course of the study we conducted approximately 100 numerical experiments. In addition we examined grid resolution issues and domain size independence. Each simulation took approximately three to ten days of CPU time depending on the computational intensity of the model approximations. Here, we report on approximately 20 of the experiments that cover our major observations in an attempt to distill our experience into approximately 20 pages to assist the community of modelers who may be interested in how similar model approximations could affect the mean alongshore current response in their models. By comparing our model predictions with the field data from the Duck experiments, the relative influence of wave-current interaction, and the bottom friction and wave-breaking parameterizations can then be quantitatively assessed.

The outline of this paper is as follows. The model formulation is described in § 2.

The effects of wave-current interaction, the bottom friction parameterization, and different wave-breaking models are presented in § 3. Finally, a summary is provided in § 4.

2 Formulation

The two-dimensional shallow water equations are used to describe the depth-averaged and time-averaged (with respect to the period of incident waves) mean flows. Forcing effects from obliquely-incident breaking surface waves are approximated by a body force in the alongshore momentum equations determined using linear radiation-stress theory. The bottom friction shear stress is assumed linear in the base case model; non-linear parameterizations are investigated in section § 3.2. Weak biharmonic friction is included to provide additional numerical stability at high wave-numbers in the finite-difference solutions. The rigid lid approximation, justified by Allen *et al.* (1996) and shown to agree closely with a free-surface approximation by Özkan-Haller & Kirby (1999), is also employed. Tidal effects, lateral mixing due to turbulence at small scales (i.e., large eddy simulations), and the dispersive three-dimensional effect of the vertical fluctuations in the current velocities are neglected (c.f. Svendsen & Putrevu, 1994) to avoid additional uncertain parameterizations and to simplify the interpretation of and isolate the effects we are investigating.

If u and v are the across-shore and alongshore components of the velocity in the x and y directions, respectively, as indicated in Fig. 1, then the governing momentum equations are

$$(hu)_x + (hy)_y = 0 \ , \tag{1}$$

and

$$
\begin{aligned}
u_t + uu_x + vu_y &= -\frac{p_x}{\rho} + \tau_x^w - \frac{C_f < |\vec{u}|u >}{h} - \nu\nabla^4 u \ , \\
v_t + uv_x + vv_y &= -\frac{p_y}{\rho} + \tau_y^w - \frac{C_f < |\vec{u}|v >}{h} - \nu\nabla^4 v \ , \qquad (2)
\end{aligned}
$$

where $\vec{u}$ is the phase-averaged current velocity vector, t is time, p is the pressure, ρ is the constant water density, $h = h(x)$ is the local water depth, ν is a biharmonic diffusion coefficient, and $<>$ indicate time-averaged quantities. Momentum input from the waves is supplied through the τ_x^w and τ_y^w terms. Energy dissipation is a function of the dimensionless bottom friction coefficient C_f. In the base model, a linear bottom friction parameterization is used with

$$
\begin{aligned}
C_f < |\vec{u}|u > &= \mu u \ , \\
C_f < |\vec{u}|v > &= \mu v \ , \qquad (3)
\end{aligned}
$$

where μ is an averaged dimensional bottom friction velocity.

For small amplitude waves in irrotational flows, Longuet-Higgins & Stewart (1960) showed that the forcing due to waves is related to the wave radiation stress tensor $S_{ij,w}$,

$$
\begin{aligned}
\tau_x^w &= -\frac{1}{\rho h}\left(\frac{\partial S_{11,w}}{\partial x} + \frac{\partial S_{12,w}}{\partial y}\right) \ , \\
\tau_y^w &= -\frac{1}{\rho h}\left(\frac{\partial S_{12,w}}{\partial x} + \frac{\partial S_{22,w}}{\partial y}\right) \ , \qquad (4)
\end{aligned}
$$

where for linear waves,

$$
S_{ij,w} = \frac{E_w}{2}\left[\frac{2C_g}{c}\frac{k_i k_j}{k^2} + \left(\frac{2C_g}{c} - 1\right)\delta_{ij}\right] \ . \qquad (5)
$$

Here, E_w is the wave energy, and k_1, k_2 are components of the wave-number k in the x and y directions. This linear approximation has been widely applied in the

surfzone with modest success. The group velocity C_g and wave phase speed c are also calculated from linear wave theory,

$$C_g = \frac{c}{2}\left(1 + \frac{2kh}{\sinh 2kh}\right) \ , \tag{6}$$

$$c = \frac{\sigma}{k} \ , \tag{7}$$

where σ is the intrinsic angular frequency of the waves. Following Yu & Slinn (2003), the evolution of the wave energy is described using the wave action equation,

$$\frac{\partial}{\partial t}\left(\frac{E_w}{\sigma}\right) + \frac{\partial}{\partial x}\left[(u + C_{g1})\frac{E_w}{\sigma}\right] + \frac{\partial}{\partial y}\left[(v + C_{g2})\frac{E_w}{\sigma}\right] = -\frac{\epsilon_w}{\sigma} \ . \tag{8}$$

The dissipation rate of wave energy ϵ_w is modelled using either the TG (Thornton & Guza, 1986) or the CT (Church & Thornton, 1993) formulations that are based on field data. The TG formulation, developed for an alongshore uniform plane beach, gives

$$\epsilon_w = \frac{3\sqrt{\pi}\rho g B^3 f_p}{16}\frac{H^5}{\gamma^2 h^3}\left\{1 - \left[1 + \left(\frac{H}{\gamma h}\right)^2\right]^{-5/2}\right\} \ , \tag{9}$$

where g is the gravitational acceleration, B is an empirical constant that accounts for various breaker intensities, $f_p = 2\pi/\sigma$ is the peak wave frequency, γ is the breaker index, and H is the rms wave height distribution for a narrow-banded wave field that can be obtained from

$$E_w = \frac{1}{8}\rho g H^2 \ . \tag{10}$$

Slinn *et al.* (2000) used the TG formulation with $B = 1.2$ and $\gamma = 0.43$. The CT formulation, developed for the barred beach at Duck, North Carolina, gives

$$\epsilon_w = \frac{3\sqrt{\pi}\rho g B^3 f_p}{16}\frac{H^3}{h}\left\{1 + \tanh\left[8\left(\frac{H}{\gamma h} - 1\right)\right]\right\}\left\{1 - \left[1 + \left(\frac{H}{\gamma h}\right)^2\right]^{-5/2}\right\} \ . \tag{11}$$

Yu & Slinn (2003) used the CT formulation with $B = 1.3$ and $\gamma = 0.38$.

The computational domain, illustrated in Fig. 1, extends between $0 \leq x \leq L^x$ and $0 \leq y \leq L^y$. The water depth h is an alongshore uniform approximation of the actual beach bathymetry measured on October 15 during the Delilah experiment (Birkemeier *et al.* (1997)). The shallow water equations require a vanishing across-shore mass flux at the shoreline and at the offshore boundary: $hu = 0$ at $x = 0$ and $x = L^x$. Periodic conditions are imposed on u, v, and p in the alongshore direction due to the nature of the alongshore uniform flow field. The biharmonic diffusion operator requires the additional boundary conditions $u_{xx} = v_x = v_{xxx} = 0$ at $x = 0$ and $x = L^x$.

The numerical scheme is described in detail by Allen *et al.* (1996). The time derivative is initially zero, and $u = v = 0$. A small random perturbation is added to the velocity field at each time step to trigger any instabilities in the flow. The biharmonic diffusion operator ν is 1.25 $\mathrm{m^4 s^{-1}}$. In all simulations, $\Delta t = 0.1$ s, and $\Delta x = \Delta y = 2.0$ m everywhere on the grid. Tests have shown that this provides grid independent solutions. The initial wave field is the steady state solution with no current. When a wave-current interaction model is used in the simulations, Eq. 8 is advanced in time using the first order Euler method and then coupled with the momentum Eq. 2 (see Yu & Slinn, 2003). When wave-current interaction is not considered, Eq. 8 is integrated at the start of the simulation in space only, using the initial conditions.

Small horizontal mixing terms τ_x' and τ_y' are added to the x and y momentum equations, respectively (Eq. 2) to increase the numerical stability of the code for

turbulent simulations when using the wave-current interaction model. We implement

$$\tau_x' = C_h \nabla^2 u \ ,$$
$$\tau_y' = C_h \nabla^2 v \ , \tag{12}$$

with $C_h = 0.25$ m^{2}s^{-1}. Our simulations utilizing smaller values or alternate formulations for $C_h = f(\nabla u, h, \epsilon_w)$ led to qualitatively similar results. For example, we tested the formulation implemented by Özkan-Haller & Kirby (1999) in their study of alongshore current instabilities, i.e.,

$$\tau_x' = \frac{2}{h}\frac{\partial}{\partial x}\left(hC_h\frac{\partial u}{\partial x}\right) + \frac{1}{h}\frac{\partial}{\partial y}\left(hC_h\frac{\partial v}{\partial x}\right) \ ,$$
$$\tau_y' = \frac{1}{h}\frac{\partial}{\partial x}\left(hC_h\frac{\partial v}{\partial x}\right) \ , \tag{13}$$

where $C_h = 0.25h\left(\epsilon_w/\rho\right)^{1/3}$. The effects of the horizontal mixing terms are investigated in the next section.

3 Parameterizations

The effects of wave-current interaction, non-linear bottom friction, and various wave-breaking models are investigated in this section by comparing model predictions with each other and with field data. The conditions reported over two four-hour periods during the Delilah experiment are considered: the moderate 0.7 m waves measured between 9:00 am and 1:00 pm on October 15th, and the large 1.5 m waves measured between 7:00 am and 11:00 am on October 13th. Both periods correspond to low tide, over which the mean water depth remained relatively constant with time. (During each 4 hour period, the water depth varied by 0.14 m on October 15th and 0.21 m on October 13th.) The model input parameters, including the offshore wave angle θ,

wave height H_o, and wave period T_p, corresponded to the time-averaged field data values, and are summarized in table 1 along with the modelled domain size.

3.1 Wave-current interaction

Yu & Slinn (2003) demonstrated that the interaction between incident waves and offshore currents on a alongshore variable beach affects the development of flow instabilities and reduces the strength and extent of the rip currents. Simulations with and without wave-current interaction predicted significantly different flow patterns. In the present study, the same wave-current interaction formulation is used to model the Delilah alongshore-uniform barred beach. The conditions measured on October 15th are modelled using a linear bottom friction parameterization with μ set arbitrarily to 0.0020 m/s. The CT barred-beach approximation is used for ϵ_w. The effect of the horizontal mixing terms that are required to maintain numerical stability when using the wave-current interaction model for these particular waves and unsteady turbulent phase-averaged flow fields are also examined.

Time series of the v velocity component at (114 m, 600 m), slightly seaward of the sandbar at $x = 100$ m, are shown in Fig. 2. Plots (a) and (b) correspond to simulations without wave-current interaction, and plots (b) and (c) correspond to simulations with constant horizontal mixing (Yu & Slinn, 2003). Although the magnitude of the mixing terms is small, they effectively smooth out some of the velocity fluctuations in the alongshore current. When the wave-current interaction model is used, the instabilities require more time to develop (35 mins rather than $15 - 20$ mins), and there is a slight additional dampening effect over that of the horizontal mixing. The time- and alongshore-averaged v velocities for simulations with constant and variable

(Özkan-Haller & Kirby, 1999) horizontal mixing as a function of the offshore distance x are shown in Fig. 3. The results are compared to the October 15th Delilah field data. Large alongshore currents with a peak value at $x = 110$ m are located offshore of the sandbar in all of the profiles. A strong alongshore current and large velocity gradients near the beach ($x < 20$ m) are also present in the simulations, but do not appear in the field data. This is an artificial result of the implicit assumption that all the wave-breaking energy is dissipated as the wave shoals. The approximation is less realistic for steeper beaches as increased wave energy is reflected offshore (see Elgar *et al.* , 1994). The magnitude of the alongshore current is similar to the field data because this was adjusted through the arbitrary bottom friction coefficient for these simulations. But the location of the current is shifted too far offshore. Wave-current interaction affects the peak values of the alongshore current: the magnitude of the artificial peak close to the shore decreases, and the magnitude of the peak seaward of the sandbar increases. While the differences are as much as 15%, the wave-current interaction model does not shift the location of the alongshore current peak and does not eliminate the artificial peak near the shore. A comparison between the results with constant and variable horizontal mixing shows velocity differences of up to 25% in the trough. However, the mixing model also does not shift the location of the alongshore current peak, as reported by Reniers & Battjes (1997). The constant horizontal mixing terms have a negligible effect on the averaged velocity profiles; therefore, a comparison between simulations with and without horizontal mixing terms is not shown in this figure.

Plots of the instantaneous vorticity field obtained from the October 15th simulations are shown in Fig. 4. These plots are used to clarify the differences between

the model predictions even though they cannot be directly compared to experimental data. The simulation without wave-current interaction or constant horizontal mixing (a) shows an irregular pattern of strong vorticity running parallel to the shore ($x < 250$ m) that propagates in the direction of the alongshore current. Vortices are shed offshore occasionally and persist in the region $x > 300$ m for $1 - 2$ hours. The flow field is similar to the lowest bottom friction case examined by Slinn *et al.* (1998). Constant horizontal mixing, present in the (b) and (c) simulations, affects the pattern of the flow instabilities at any given time. The vorticity is reduced and mostly concentrated into four bands that run parallel to the shore: one on either side of the sandbar, and two right next to the shoreline. Few vortices are shed offshore, and those that do detach from the outer two bands dissipate quickly. Wave-current interaction adds to the effect of the horizontal mixing, and also increases the magnitude and variability of areas of high vorticity immediately next to the shoreline (see $y = 650$ m in (c)). This is confirmed by plots of time- and alongshore-averaged turbulent kinetic energy densities ($\frac{1}{2} < \overline{u'^2} + \overline{v'^2} >$, where $\overline{u'^2}$ and $\overline{v'^2}$ are alongshore-averaged quantities) as a function of offshore distance, shown in Fig. 5. The level of turbulent kinetic energy is sharply reduced by the constant horizontal mixing, and further reduced over the sandbar by wave-current interaction.

Although the wave-current interaction model affects the dynamics of the turbulence, it does not eliminate the large artificial alongshore current peak near the shore. We note that the model also requires twice the length of time to compute a given numerical simulation when wave-current interaction is included. In the following sections, we seek combinations of model features that will act to improve the mean alongshore current predictions and reduce the magnitude of the artificial

shoreline peak. Therefore, the majority of the remaining simulations do not use the wave-current interaction model or the stability-enhancing horizontal mixing terms but focus on the isolated influence of other parameterizations. Our approach differs from that of Bühler & Jacobson (2001), who demonstrated that a nonhomogeneous wavetrain tends to shift the alongshore current peak shorewards.

3.2 Bottom friction

Feddersen *et al.* (2000) used measurements from the Duck94 field experiment to evaluate the accuracy of various bottom friction parameterizations. They concluded that linear parameterizations did not produce results that were consistent with the field data. In this section, we consider four different bottom friction parameterizations and examine their effect on the unsteady alongshore current predictions.

The bottom friction is modelled using the $< |\vec{u}|u >$ and $< |\vec{u}|v >$ stress terms in Eq. 2. The linear parameterization used in § 3.1 is given by Eq. 3. A non-linear parameterization is obtained when both velocities in each stress term are evaluated using the modelled data. Here we consider explicitly that the total instantaneous velocities (u_{tot}, v_{tot}) in the nearshore consist of the sum of the phase-averaged current (u, v) and wave (u_w, v_w) velocities:

$$\begin{aligned} u_{tot} &= u + u_w \ , \\ v_{tot} &= v + v_w \ . \end{aligned} \tag{14}$$

The u_w and v_w components of the velocities have been neglected generally throughout the manuscript. We note, however, that the wave induced near-bottom currents can have a significant effect in the bottom friction parameterization. The magnitude of

the cross shore velocity is therefore

$$|\vec{u_{tot}}| = \left[(u_c + u_w)^2\right]^{1/2} \quad . \tag{15}$$

The wave velocity can be expressed as

$$\begin{aligned} u_w &= u_o \cos(\theta)\cos(\omega t) \ , \\ v_w &= u_o \sin(\theta)\cos(\omega t) \ , \end{aligned} \tag{16}$$

where ω is the radian frequency and u_o is the orbital velocity in shallow water,

$$u_o(x,y) = \frac{H\sigma}{2}\frac{1}{\sinh(kh)} \ . \tag{17}$$

Integrating across a wave period gives

$$\begin{aligned} < |\vec{u}|u > &= \frac{1}{T}\int_T \left[u_o^2\cos^2(\omega t) + 2u_o\cos(\omega t)(u_c\cos\theta + v_c\sin\theta) + u_c^2 + v_c^2\right]^{1/2} \\ &\qquad [u_c + u_o\cos\theta\cos(\omega t)]\,dt \ , \\ < |\vec{u}|v > &= \frac{1}{T}\int_T \left[u_o^2\cos^2(\omega t) + 2u_o\cos(\omega t)(u_c\cos\theta + v_c\sin\theta) + u_c^2 + v_c^2\right]^{1/2} \\ &\qquad [v_c + u_o\sin\theta\ \cos(\omega t)]\,dt \ . \end{aligned} \tag{18}$$

These integrals are evaluated numerically using Simpson's rule with 16 intervals.

The above integrals require considerable computational effort to evaluate, so alternate non-linear bottom friction parameterizations have been proposed. Feddersen *et al.* (2000) recommend the WT parameterization originally proposed by Wright & Thompson (1983),

$$\begin{aligned} < |\vec{u}|u > &= \sigma_T u\left[\alpha^2 + \left(\frac{u}{\sigma_T}\right)^2\right]^{1/2} \ , \\ < |\vec{u}|v > &= \sigma_T v\left[\alpha^2 + \left(\frac{v}{\sigma_T}\right)^2\right]^{1/2} \ , \end{aligned} \tag{19}$$

where σ_T is the square root of the total velocity variance, and can be approximated by $\sigma_T \approx [u_o/2]^{1/2}$. They found that $\alpha = 1.16$ gives good agreement with experimental data for alongshore currents.

The dimensionless drag coefficient C_f can be set to a constant, or parameterized with the Manning-Strickler equation following Ruessink *et al.* (2001):

$$C_f = 0.015 \left(\frac{k_a}{h} \right)^{1/3} \tag{20}$$

where the apparent bed roughness k_a is assumed to be constant and time-independent.

The effects of the bottom friction parameterization on the predicted time- and alongshore-averaged v velocity are shown in Fig. 6. The four cases shown use the Eq. 3 linear parameterization with $\mu = 0.0020$ ms^{-1}, the Eq. 18 integral parameterization with constant $C_f = 0.0030$, the Eq. 19 WT correlation with constant $C_f = 0.0030$, and the Eq. 19 WT correlation with constant bed roughness $k_a = 0.018$. The CT wave-breaking model is used with the October 15th Delilah conditions in all of the simulations shown in the figure. The adjustable μ, C_f, and k_a parameters are set to give peaks of approximately equal height at $x = 110$ m.

Figure 6 indicates that non-linear bottom friction parameterizations have a large effect on the predictions close to the shore. Although the non-linear bottom friction parameterizations reduce the artificially high magnitude of the alongshore current at $x < 20$ m, the strong currents and velocity gradients persist. There is a slight difference of up to 10% between the two non-linear parameterizations, and simulations using the WT correlation run twice as fast as those using the integral parameterization. The simulations with a constant bed roughness and variable C_f give slightly higher alongshore currents for $x > 100$ m and slightly lower alongshore currents for

$x < 50$ m.

Since the non-linear bottom friction parameterizations are expected to more closely approximate field conditions, the WT correlation with constant bottom friction is used for the remainder of the simulations.

3.3 Wave-breaking model

The wave-breaking model controls the amount of wave energy that is converted into flow momentum in the nearshore water column through the radiation stress gradients. As a wave moves towards the shore and breaks, the alongshore current increases and the wave height decreases. A comparison of the wave heights predicted using the TG and the CT wave-breaking models with both the October 15th and 13th Delilah conditions is shown in Fig. 7. Both models perform well with the moderate waves of October 15th, but under-predict the large waves of October 13th by as much as 35% between $0 < x < 100$ m. Since the CT model was tuned using the Delilah experimental data, it predicts the local wave height $H(x)$ somewhat better. The corresponding time- and alongshore-averaged alongshore current predictions for the October 15th conditions are shown in Fig. 8. The predicted average alongshore current obtained using either wave-breaking model exhibits the same problems described in § 3.1, even though both models predicted the wave heights well. There is little advantage of using one model over the other.

A roller model was added to the wave-breaking model to address discrepancies between the predictions and field data. Roller models store the energy dissipated from breaking waves and release it closer to the shore as the roller becomes smaller. Consequently, the wave momentum is imparted into the water column shoreward of

the location of wave breaking and the alongshore current is shifted shoreward. If the roller model is formulated so that a finite roller energy is permitted at the shore to account for wave reflections, the artificial alongshore current peak at $x = 20$ can also be reduced or eliminated.

In this section, we assume that the roller is part of the wave and remains attached to the wave as it breaks. The roller energy therefore acts as a storage term for the wave energy.

Reniers & Battjes (1997) included a second one-dimensional energy equation in their roller model to account for the roller energy E_r. When extended to a two-dimensional time-dependent formulation, the roller energy equation is similar to the wave energy Eq. 8,

$$\frac{\partial}{\partial t}\left(\frac{E_r}{\sigma}\right) + \frac{\partial}{\partial x}\left[(u + C_{g1})\frac{E_r}{\sigma}\right] + \frac{\partial}{\partial y}\left[(v + C_{g2})\frac{E_r}{\sigma}\right] = \frac{\epsilon_w}{\sigma} - \frac{\epsilon_r}{\sigma} \quad . \tag{21}$$

The equation contains a source term ϵ_w/σ equal to the dissipation from the wave energy equation, and a sink term that is a function of ϵ_r, the dissipation rate of the roller energy. The dissipation rate is modelled as the work performed by the shear stress τ_r between the roller and the organized wave motion (Deigaard & Fredsoe, 1989),

$$\epsilon_r = \tau_r c \quad . \tag{22}$$

Following Nairn *et al.* (1990), the shear stress is deduced by considering the vertical force balance on the roller. This gives

$$\epsilon_r = \rho g \frac{A_r}{T} \sin\beta \quad , \tag{23}$$

where A_r is the cross-sectional area of the roller and β is the angle of the wave-roller stress vector. Lippmann *et al.* (1996) showed that the model is insensitive to values

of $\beta > 10^o$; $\beta = 10^o$ was used in the present study. The roller energy is coupled to the shallow water equations (Eq. 2) through the wave forcing terms in Eq. 4 in the same manner as the wave energy,

$$\begin{aligned} \tau_x^w &= -\frac{1}{\rho h}\left(\frac{\partial S_{11,w}}{\partial x} + \frac{\partial S_{12,w}}{\partial y} + \frac{\partial S_{11,r}}{\partial x} + \frac{\partial S_{12,r}}{\partial y}\right) \ , \\ \tau_y^w &= -\frac{1}{\rho h}\left(\frac{\partial S_{12,w}}{\partial x} + \frac{\partial S_{22,w}}{\partial y} + \frac{\partial S_{12,r}}{\partial x} + \frac{\partial S_{22,r}}{\partial y}\right) \ , \end{aligned} \tag{24}$$

where the formulation of the roller radiation stresses $S_{ij,r}$ is similar to the wave energy stresses,

$$S_{ij,r} = \frac{E_r}{2}\left[\frac{2C_g}{c}\frac{k_i k_j}{k^2} + \left(\frac{2C_g}{c} - 1\right)\delta_{ij}\right] \ . \tag{25}$$

The roller energy is set to zero offshore, and Eq. 21 is integrated in space towards the shore. E_r remains zero until the waves break and the wave energy begins to dissipate ($\epsilon_w > 0$). No boundary condition is prescribed for E_r at the shore, so the roller energy can have a positive value at $x = 0$ provided that it has not been entirely dissipated.

The remaining unknown quantity in the roller model is the roller area A_r. Several formulations have been proposed. Lippmann *et al.* (1996) used the Engelund relation,

$$A = \frac{H_b^3}{4h\tan\beta} \ , \tag{26}$$

where H_b is the wave height at the onset of breaking. Svendsen (1984) used

$$A = 0.9H^2 \ . \tag{27}$$

These formulations are plotted in Fig. 9 as functions of the offshore distance x using the October 15th Delilah conditions and the CT wave-breaking model. Between $30 < x < 100$ m, the Engelund/Lippmann and Svendsen roller areas are within 15% of each other. The two roller areas differ considerably in other regions. In particular,

the Engelund/Lippmann formulation does not approach zero at the shoreline. Both formulations give $A_r \neq 0$ in deep water; this does not affect the roller model since E_r remains zero until the wave energy starts to dissipate, i.e., negative values of E_r are not permitted in the model.

The roller model is tested with the Engelund/Lippmann and Svendsen roller areas, and with a new formulation based on E_r,

$$A_r = C_1 E_r \quad , \tag{28}$$

where the constant $C_1 = 0.75$ gives roller areas similar to the Engelund/Lippmann and Svendsen formulations between $80 < x < 100$ m. Equation 28 gives large values of A_r as $x \to 0$. Therefore, nearly all of the roller energy will dissipate as the waves shoal, and the artificial alongshore current peak at $x \approx 20$ m will remain in the predictions. To eliminate the peak, Eq. 28 is replaced over the region $0 < x < 25$ m with a linear relation that goes to zero as $x \to 0$. This transfers the roller energy to the alongshore current. The resulting roller area, both with and without the linear damping near the shoreline, is plotted in Fig. 9. To verify the model findings, an "ideal" roller area is also used, for which a third-order polynomial curve is fitted to the alongshore current field data shown in Fig. 8. Then Eq. 21 can be used to determine an optimum roller area that would most closely produce the observed alongshore currents assuming negligible $\partial u/\partial x$, $\partial u/\partial y$, and $\partial v/\partial y$ gradients, steady flow, and linear bottom friction. Using the October 15th Delilah conditions, this gives

$$A_{r,ideal} = 8.238 \times 10^{-7} x^3 - 2.809 \times 10^{-4} x^2 + 2.543 \times 10^{-2} x - 3.468 \times 10^{-1} \tag{29}$$

between $17 < x < 123$ m, and zero elsewhere. The ideal roller area described by Eq. 29 is only valid for the October 15th Delilah conditions. The point of this exercise is

simply to demonstrate that by using a roller formulation, some ideal definition of the roller area could exist in principle to couple the location of momentum input from the breaking waves to the mean currents using standard linear theory through radiation stress gradients and wave energy dissipation parameterizations. The cross-shore distribution of the "ideal" roller area for this case is shown only to suggest that the order of magnitude of the roller area is approximately correct for each of the three standard roller formulations in the key region $20 < x < 120$ m. Also, the "ideal" area result shows that the near shore tendency of the Svendsen formulation, for $A_r \to 0$ as $x \to 0$, is a model feature that will tend to produce cross-shore profiles of the alongshore current that do not exhibit as large of a nearshore jet.

The wave and roller energy as a function of the across-shore distance x for each roller model are shown in Fig. 10(a). The plot indicates that rollers begin to form at approximately $x = 140$ m, 40 m offshore from the sandbar. All roller models except the one based on the Engelund/Lippmann formulation contain some roller energy at the shore. The corresponding values of the y-forcing term τ_y^f in Eq. 24 are shown in Fig. 10(b). Sharp peaks in the forcing profiles appear near the shore when the Engelund/Lippmann formulation is used. The Svendsen formulation gives a peak at the point where the waves start to break. The linear relation combined with the $A_r = C_1 E_r$ formulation eliminates the sharp peak in its forcing profile near the shore. As expected, the "ideal" roller area gives a smooth forcing profile similar in shape to the velocity profile described by Eq. 29.

The time- and alongshore-averaged alongshore current predictions with the different roller model formulations are shown in Fig. 11. The simulations use the CT wave-breaking model without wave-current interaction or horizontal mixing, and the

WT bottom-friction correlation with constant $C_f = 0.0030$. The results obtained using the October 15th Delilah field conditions are shown in (a). The solid line gives the results obtained without a roller model. In Fig. 11(a), the Engelund/Lippmann roller area formulation shifts the alongshore current peak at $x = 120$ m shorewards to $x = 90$ m, but does not reduce the size of the artificial peak at $x = 20$ m since wave energy is not stored in this region. The Svendsen roller area reduces the size of the artificial peak, but does not shift the location of the alongshore current peak. The roller area formulation based on the roller energy shifts the alongshore current peak to $x = 90$ m and eliminates the artificial peak at $x = 20$ m because the roller area is forced to zero at $x = 0$. The "ideal" roller area curve is shifted the farthest to $x = 60$ m, and is closest to the field data. This is to be expected since the ideal area was based on the field data. The magnitude of the alongshore current is slightly over-predicted with the ideal roller area and the peak is not shifted shoreward enough as a result of the simplifying assumptions made when it was formulated. The curve obtained using roller area based on the roller energy is the closest to the ideal roller area curve, and is therefore recommended for future roller model applications. The roller model improvements are also apparent when the October 13th Delilah conditions are modelled (see Fig. 11(b)). The trough at $x = 55$ m is eliminated, and the alongshore current peak is closer to that of the field data. Farther offshore, however, the alongshore current is under-predicted. This can be fixed by using $C_f = 0.0020$, as shown in Fig. 12. However, the discrepancy between the predictions and field data is likely due to the incorrect wave height predictions from the wave-breaking model, as shown in Fig. 7.

Plots of instantaneous vorticity using the roller model with each roller area formu-

lation are shown in Fig. 13 for the October 15th Delilah conditions. A plot obtained without using the roller model is also shown for comparison in (a). Results obtained using the following roller areas are given: the Engelund/Lippmann (b), the Svendsen (c), the roller area based on the roller energy with nearshore damping (d), and the ideal roller area (e). The roller model reduces the alongshore instabilities in the flow field because the cross-shore forcing gradient is decreased seaward of the sandbar, regardless of the roller area used (see Fig. 10(b)). The smallest forcing gradients correspond to the ideal and Engelund/Lippmann roller areas; the flows simulated using these formulations do not shed vortices from the alongshore current when the October 15th Delilah conditions are modelled. Small vortices are shed when the Svendsen or the roller energy formulations are used. The same patterns are evident when the October 13th Delilah conditions are modelled, shown in Fig. 14. The results with no roller model is plotted in (a), and the results with the roller area based on the roller energy and either $C_f = 0.0030$ or $C_f = 0.0020$ are plotted in (b) and (c), respectively. When the bottom friction coefficient is lowered, weak vortex patterns appear in the alongshore current. However, vortices are not shed from the alongshore current in either plot.

A roller model with an appropriate roller area shifts the alongshore current shorewards and eliminates the artificial peak close to the shore to better match the field data. This cannot be achieved by modifying other code parameters. The best roller area tested is based on the roller energy, with $A_r = C_1 E_r$ and $C_1 = 0.75$ when $x > 25$ m. A linear relation that goes to zero as $x \to 0$ is used between $0 < x < 25$ m.

4 Summary and Future Work

The two-dimensional shallow water equations were used to model the alongshore currents over a barred beach for conditions measured during two days of the Delilah field experiment. The results were compared with field data to quantify the effects of different models and parameterizations. The inclusion of a roller model had the greatest effect on the results and improved the predictions significantly, provided that an appropriate roller area was used. The non-linear bottom friction model affected the predictions shoreward of the sandbar when compared to a linear model, but did not shift the predicted location of the peak alongshore current. Wave-current interaction had a lesser effect on the mean flow results.

The numerical code used for the present study has been tested for two different days at a single beach. However, it relies on a highly empirical dissipation of wave energy correlation that was formulated for the same beach. Thus, variable results might be expected when different beach topographies are modelled. In the future, the recommended alongshore current model needs to be compared against field data for different beach bathymetries to indicate the level of confidence that can be ascribed to the present predictions.

References

Allen, J. S., Newberger, P. A., & Holman, R. A. 1996. Nonlinear shear instabilities of alongshore currents on plane beaches. *J. Fluid Mech.*, **310**, 181–213.

Birkemeier, W. A., Donoghue, C., Long, C. E., Hathaway, K. K., & Baron, C. F. 1997. *The DELILAH nearshore experiment: Summary data report.* Tech. rept. US Army Corps of Engineers, Waterways Experiment Station, Vicksburg, MS.

Bowen, A. J., & Holman, R. A. 1989. Shear instabilities of the mean longshore current, 1. Theory. *J. Geophys. Res.*, **94**(C12), 18023–18030.

Bühler, O., & Jacobson, T. E. 2001. Wave-driven currents and vortex dynamics on barred beaches. *J. Fluid Mech.*, **449**, 313–339.

Church, J. C., & Thornton, E. B. 1993. Effects of breaking wave induced turbulence within a longshore current model. *Coastal Eng.*, **20**, 1–28.

Deigaard, R., & Fredsoe, J. 1989. Shear stress distribution in dissipative water waves. *Coastal Eng.*, **13**, 357–378.

Elgar, S., Herbers, T. H. C., & Guza, R. T. 1994. Reflection of ocean surface gravity waves from a natural beach. *J. Phys. Oceanogr.*, **24**, 1503–1511.

Feddersen, F., Guza, R. T., Elgar, S., & Herbers, T. H. C. 2000. Velocity measurements in alongshore bottom stress parameterizations. *J. Geophys. Res.*, **105**(C4), 8673–8686.

Lippmann, T. C., Brookins, A. H., & Thornton, E. B. 1996. Wave energy transformation on natural profiles. *Coastal Eng.*, **27**, 1–20.

Longuet-Higgins, M. S., & Stewart, R. W. 1960. The changes in the form of short gravity waves on steady non-uniform currents. *J. Fluid Mech.*, **8**(C12), 565–583.

Nairn, R. B., Roelvink, J. A., & Southgate, H. N. 1990. Transition zone width and implications for modelling surfzone hydrodynamics. *Pages 68–81 of:* Edge, B. L. (ed), *Proc. 22nd Coastal Engineering Conference*. ASCE.

Oltman-Shay, J., Howd, P. A., & Birkemeier, W. A. 1989. Shear instabilities of the mean longshore current, 2. Field data. *J. Geophys. Res.*, **94**(C12), 18031–18042.

Özkan-Haller, H. T., & Kirby, J. T. 1999. Nonlinear evolution of shear instabilities of the longshore current: A comparison of observations and computations. *J. Geophys. Res.*, **104**(C11), 25953–25984.

Reniers, A. J. H. M., & Battjes, J. A. 1997. A laboratory study of longshore currents over barred and non-barred beaches. *Coastal Eng.*, **30**, 1–22.

Ruessink, B. G., Miles, J. R., Feddersen, F., Guza, R. T., & Elgar, S. 2001. Modeling the alongshore current on barred beaches. *J. Geophys. Res.*, **106**(C10), 22451–22463.

Slinn, D. N., Allen, J. S., Newberger, P. A., & Holman, R. A. 1998. Nonlinear shear instabilities of alongshore currents over barred beaches. *J. Geophys. Res.*, **103**(C9), 18357–18379.

Slinn, D. N., Allen, J. S., & Holman, R. A. 2000. Alongshore currents over variable beach topography. *J. Geophys. Res.*, **105**(C7), 16971–16998.

Svendsen, I. A. 1984. Wave heights and set-up in a surf zone. *Coastal Eng.*, **8**, 303–329.

Svendsen, I. A., & Putrevu, U. 1994. Nearshore mixing and dispersion. *Proc. Royal Soc. London A*, **445**, 561–576.

Thornton, E. B., & Guza, R. T. 1986. Surf zone longshore currents and randon waves: Field data and models. *J. Phys. Oceanogr.*, **16**, 1165–1178.

Wright, D. G., & Thompson, K. R. 1983. Time-averaged forms of the nonlinear stress law. *J. Phys. Oceanogr.*, **13**, 341–346.

Yu, J., & Slinn, D. N. 2003. Effects of wave-current interaction on rip currents. *J. Geophys. Res.*, **108**(C3).

Delilah conditions	L^x(m)	L^y(m)	$\theta(^o)$	H_o(m)	T_p(s)
October 15	600	1200	39.1	0.707	10.76
October 13	1000	1200	48.2	1.540	11.34

Table 1: Input parameters

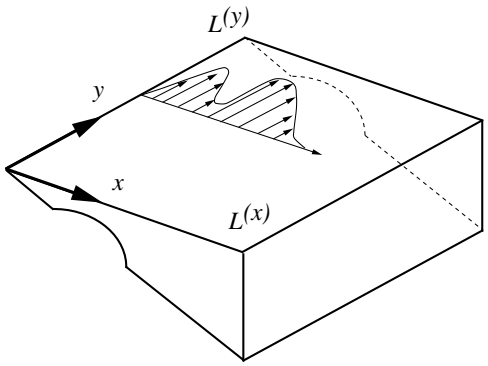

Figure 1: Modelled geometry.

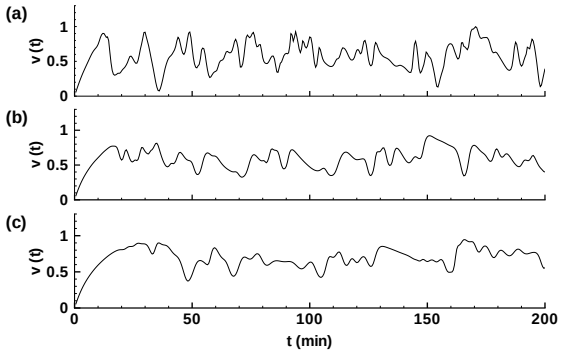

Figure 2: Predicted October 15th alongshore velocity time-series at (114m, 600m) (a) without wave-current interaction or horizontal mixing, (b) without wave-current interaction and with horizontal mixing, and (c) with wave-current interaction and horizontal mixing.

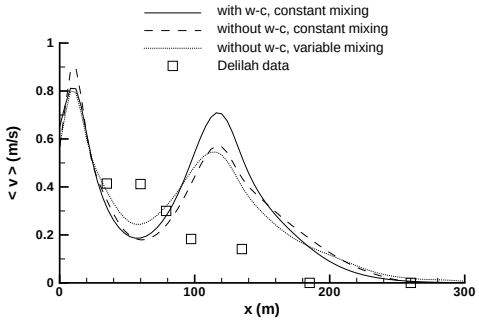

Figure 3: Time-averaged alongshore current with and without wave-current (w-c) interaction using different horizontal mixing parameterizations for the Delilah conditions measured on October 15th.

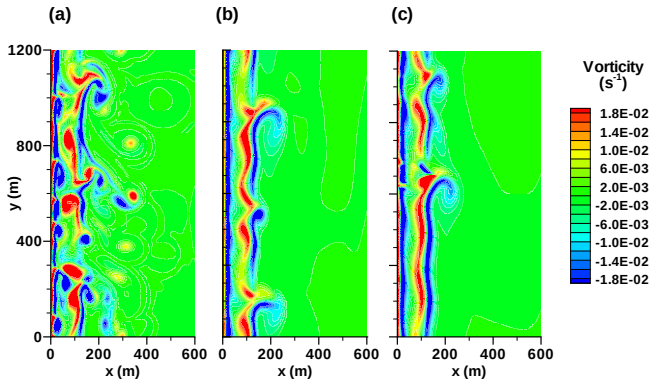

Figure 4: Instantaneous vorticity field (a) without wave-current interaction, no horizontal mixing, (b) without wave-current interaction, constant horizontal mixing, and (c) with wave-current interaction, constant horizontal mixing.

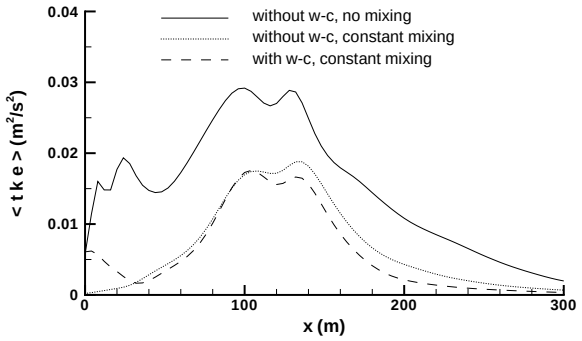

Figure 5: Time-averaged alongshore turbulent kinetic energy density with and without wave-current (w-c) interaction and constant horizontal mixing parameterization.

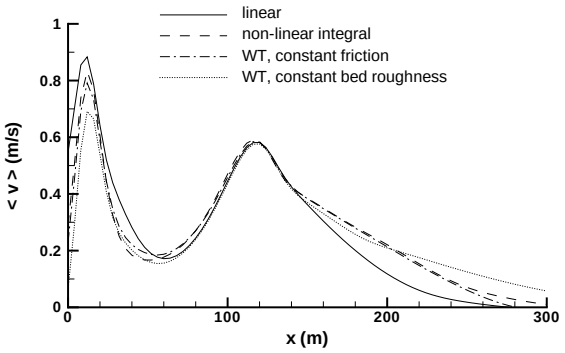

Figure 6: Time- and alongshore-averaged alongshore currents for different bottom friction parameterizations.

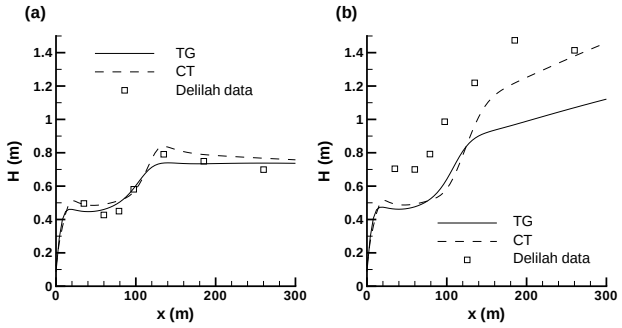

Figure 7: Predicted wave heights using the TG and CT wave-breaking models with (a) the moderate Delilah waves of October 15th and (b) the large Delilah waves of October 13th.

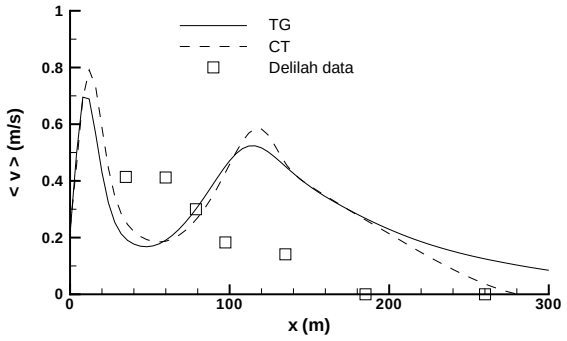

Figure 8: Predicted time- and alongshore-averaged alongshore currents using the TG and CT wave-breaking models.

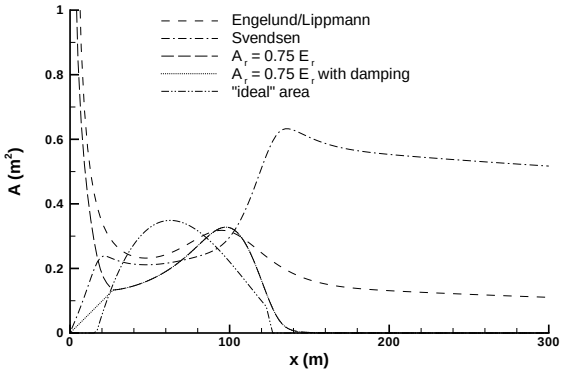

Figure 9: Roller cross-sectional areas tested in the model.

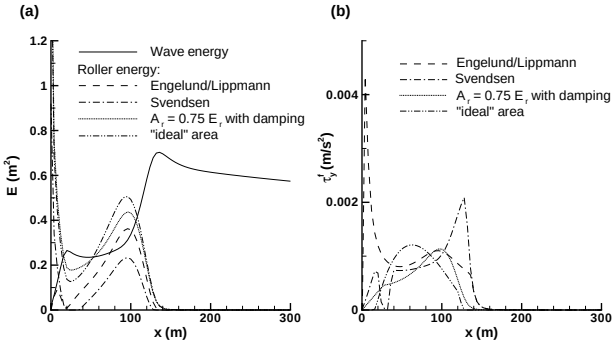

Figure 10: (a) Wave and roller energies for each roller area and (b) their corresponding alongshore forcing terms.

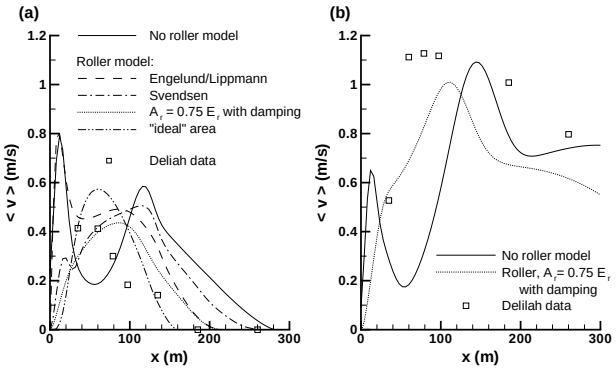

Figure 11: Time- and alongshore-averaged alongshore current predictions with and without the roller models using the (a) October 15th and (b) October 13th Delilah field conditions.

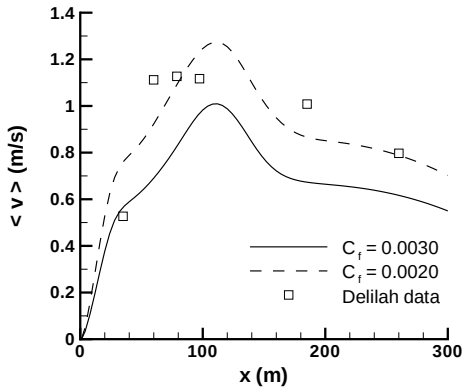

Figure 12: Predicted time- and alongshore-averaged alongshore currents using the October 13th Delilah conditions.

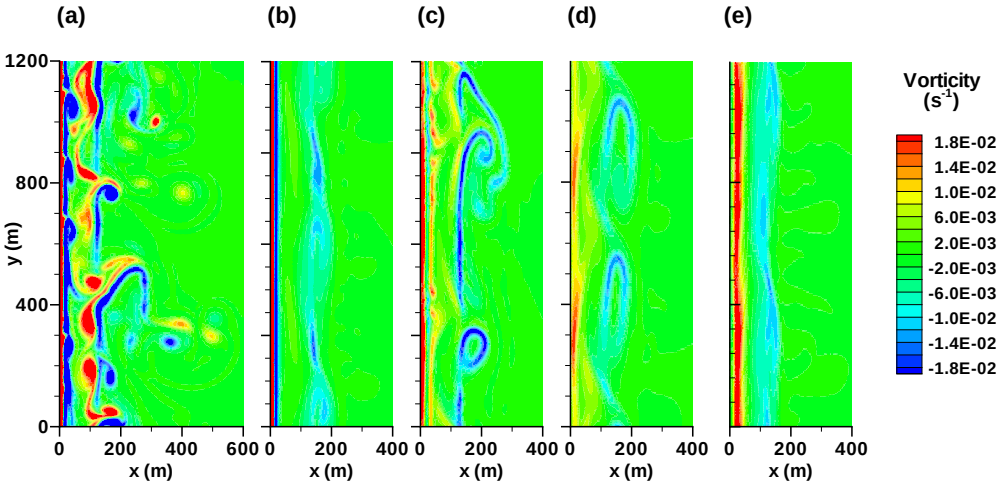

Figure 13: Instantaneous vorticity predictions using the October 15th Delilah conditions for (a) no roller model, and for roller models with (b) the Engelund/Lippmann roller area, (c) the Svendsen roller area, (d) $A_r = C_1 E_r$ with nearshore damping, and (e) the "ideal" roller area.

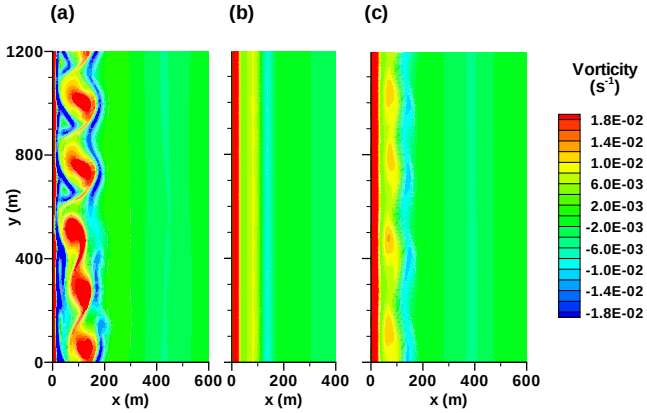

Figure 14: Instantaneous vorticity predictions using the October 13th Delilah conditions with (a) no roller model and $C_f = 0.0030$, (b) the roller model with $A_r = C_1 E_r$ and nearshore damping with $C_f = 0.0030$, and (c) the roller model with $A_r = C_1 E_r$ and nearshore damping with $C_f = 0.0020$.